JACS
JOURNAL OF THE AMERICAN CHEMICAL SOCIETY

Communication

pubs.acs.org/JACS

Oxygen Vacancies Confined in Ultrathin Indium Oxide Porous Sheets for Promoted Visible-Light Water Splitting

Fengcai Lei, Yongfu Sun,* Katong Liu, Shan Gao, Liang Liang, Bicai Pan, and Yi Xie*

Hefei National Laboratory for Physical Sciences at Microscale, Collaborative Innovation Center of Chemistry for Energy Materials, University of Science & Technology of China, Hefei, Anhui 230026, P.R. China

Supporting Information

ABSTRACT: Finding an ideal model for disclosing the role of oxygen vacancies in photocatalysis remains a huge challenge. Herein, O-vacancies confined in atomically thin sheets is proposed as an excellent platform to study the O-vacancy−photocatalysis relationship. As an example, O-vacancy-rich/-poor 5-atom-thick In_2O_3 porous sheets are first synthesized via a mesoscopic-assembly fast-heating strategy, taking advantage of an artificial hexagonal mesostructured In-oleate complex. Theoretical/experimental results reveal that the O-vacancies endow 5-atom-thick In_2O_3 sheets with a new donor level and increased states of density, hence narrowing the band gap from the UV to visible regime and improving the carrier separation efficiency. As expected, the O-vacancy-rich ultrathin In_2O_3 porous sheets-based photoelectrode exhibits a visible-light photocurrent of 1.73 mA/cm^2, over 2.5 and 15 times larger than that of the O-vacancy-poor ultrathin In_2O_3 porous sheets- and bulk In_2O_3-based photoelectrodes.

Solar hydrogen production can help to overcome the energy crisis caused by the depletion of fossil fuels and the serious environmental problems accompanying their combustion.[1] Yet, to date, the overall photoconversion efficiency is still very low and requires further promotion for commercialization. The efficiency of water splitting could be mainly limited by the following two reasons: (1) the majority of photocatalysts mainly harvests UV light, which is only 4% in the solar spectrum; (2) the photocatalysts usually possess sluggish carrier transport and low carrier separation efficiency.[2] As such, it is highly desirable to fundamentally improve the sunlight harvesting and charge-carrier separation/transport process of the photocatalysts. Recently, O-vacancies (V_O) in oxide semiconductors have been reported to increase solar light harvesting through narrowing the band gap and also serve as the active sites to improve the carrier separation efficiency, thus finally achieving improved water splitting efficiency.[3] However, the atomic-level insights into the role of O-vacancies during the photocatalytic process is still an open question. This is mainly caused by the lack of an ideal model that matches well with the real catalyst, and hence the knowledge gained from the conventional models cannot be directly applicable to the real catalysts.

Herein, conceptually new O-vacancies confined in atomically thin sheets is first presented as an ideal material model for disclosing atomic-level insights into the role of O-vacancies in photocatalysis. Taking the typical oxide semiconductor cubic-In_2O_3 as an example (Figure S1A),[4] a perfect 5-atom-thick In_2O_3 slab and oxygen-defect 5-atom-thick In_2O_3 slab with O-vacancies are initially built and density functional theory calculations are implemented to study the effect of O-vacancies on the electronic structure. Evidently, as displayed by the calculated density of states (DOS) in Figure 1B and C, the perfect 5-atom-thick In_2O_3 slab shows an obviously increased DOS at the conduction band edge compared with the bulk counterpart, which indicates that more carriers can be effectively transferred to the conduction band minimum (CBM) of the atomically thin perfect In_2O_3 sheets.[1c−e,5] Moreover, as displayed in Figures 1A and S1B, the presence of O-vacancies endows the 5-atom-thick In_2O_3 slab with obviously increased DOS at valence band maximum (VBM), which could be further demonstrated by the

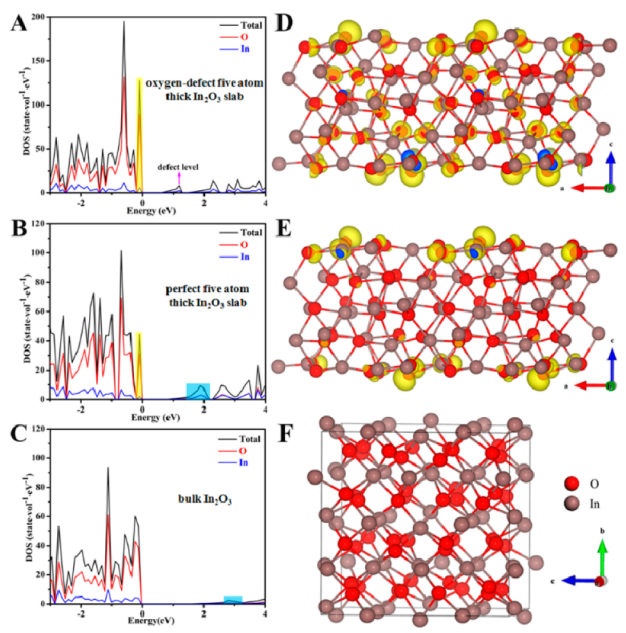

Figure 1. Calculated DOS of (A) oxygen-defect 5-atom-thick In_2O_3 slab, (B) perfect 5-atom-thick In_2O_3 slab, and (C) bulk In_2O_3. Charge density contour plots for the valence band maximum of (D) oxygen-defect 5-atom-thick In_2O_3 slab, (E) perfect 5-atom-thick In_2O_3 slab. (F) Crystal structure of In_2O_3.

Received: February 21, 2014
Published: April 28, 2014

   dx.doi.org/10.1021/ja501866r | J. Am. Chem. Soc. 2014, 136, 6826−6829

corresponding orbital wave functions in Figure 1D and E. More importantly, a new defect level appears in the oxygen-defect 5-atom-thick In_2O_3 slab, which could be ascribed to the presence of O-vacancies.[4a,6] In this case, the electrons can easily be thermally excited into the conduction band under irradiation of solar light, thereby achieving higher photoconversion efficiency. Furthermore, from the spatial distribution of the orbital wave functions at VBM displayed in Figure 1D and E, one can clearly see that the vast majority of charge density concentrates on the surface of the 5-atom-thick In_2O_3 slab. As such, the photoexcited electron−hole pairs would spend less time reaching the surface than those generated deep within the bulk In_2O_3, thus decreasing their recombination rates.

Enlightened by the above analysis, controllable synthesis of atomically thin In_2O_3 sheets with O-vacancies is highly desirable to improve the solar water splitting efficiency. Previous study shows that lattice oxygen could be released in the form of O_2 during the phase transformation from $In(OH)_3$ to In_2O_3, which leads to the formation of O-vacancies.[4a] In addition, our recent work demonstrates a novel "ultrafast open space transformation" strategy that can realize the transformation from ultrathin $CeCO_3OH$ sheets to ultrathin CeO_2 sheets.[7] This inspires us to pursue the synthesis of a suitable precursor such as ultrathin $In(OH)_3$ sheets and, hence, utilize a similar fast-heating strategy for fabricating ultrathin In_2O_3 sheets with O-vacancies. However, for the nonlayered cubic-$In(OH)_3$ without anisotropy,[8] the fabrication of their ultrathin 2D sheets is extremely challenging owing to the lack of intrinsic driving force for 2D anisotropic growth.[1c,5,9] In this work, we highlight the first synthesis of ultrathin cubic-$In(OH)_3$ sheets through a mesoscopic-assembly strategy and hence realize the fabrication of 5-atom-thick In_2O_3 porous sheets with O-vacancies via a fast-heating strategy. The number of oleate ions and their peculiar arrangement play a crucial role in the formation of ultrathin $In(OH)_3$ 2D sheets (Figure 2A): initially, three oleate ions interact with one In^{3+} ion to form an In-oleate complex via an electrostatic interaction, and the homogeneously dispersed oleate ions on the surface of In^{3+} ions lead the complex to take on a hexagonal mesostructure, in which all the In^{3+} ions are uniformly separated by one oleate ion. Meanwhile, the corresponding small-angle XRD pattern in Figure 2B demonstrates the presence of a hexagonal mesophase with a = 27.7 Å, which fairly consists with the length of one oleate ion,[10] supporting that the uniform dispersion of oleate ions on the surface of In^{3+} ions contributes to the formation of the hexagonal mesostructure. Upon hydrothermal treatment, the parallel pearl-necklace-shaped rods in the hexagonal mesostructure tend to assemble together along one direction (Figure 2A), predominantly due to the reduction of surface energy.[11] This unavoidably leads the oleate ions to rearrange on the surface of In^{3+} ions to take on Y-shaped rearrangement.0[12] When these Y-shaped arranged oleate ions align in alternative positions, a lamellar mesostructure with layer spacing of about the length of an oleate ion bilayer could be formed. This can be confirmed by the corresponding small-angle XRD pattern obtained at 2.2 h (Figure 2B), which shows a layer spacing of ca. 48.1 Å that is roughly twice the oleate ion length. After a reaction of 3 h, the finally obtained ultrathin $In(OH)_3$ sheets do not possess an ordered structure (Figures S2−S3), suggesting that the lamellar mesostructure gradually fuses into the dispersed ultrathin $In(OH)_3$ sheets (Figure 2A), further demonstrated by the small-angle XRD patterns in Figure 2B which show the gradually disappearing ordering of the mesostructure. After fast heating at 400 °C for 3 min, the decomposition of $In(OH)_3$ results in the

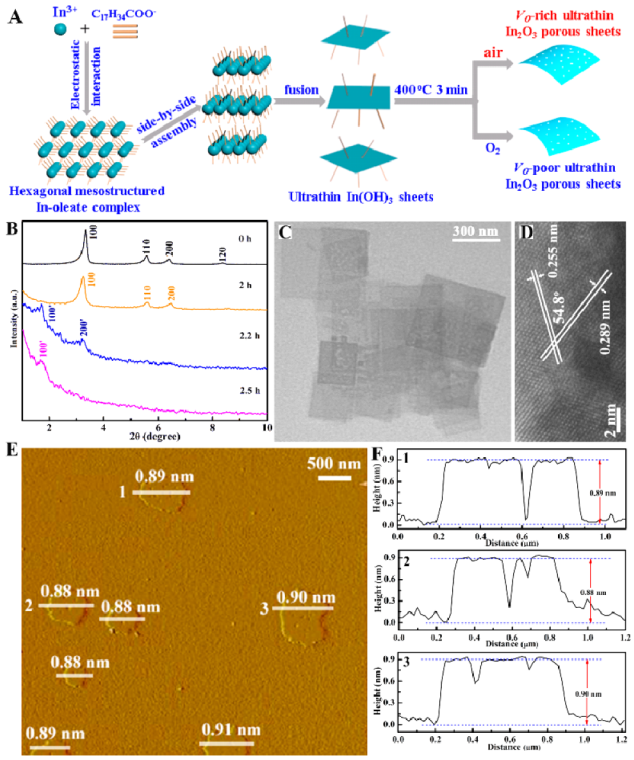

Figure 2. (A) Schematic illustration for the formation of V_O-rich/poor atomically thin In_2O_3 porous sheets at different atmosphere; (B) time-dependent small-angle XRD patterns for the as-obtained precursors; (C−F) characterizations for the V_O-rich atomically thin In_2O_3 porous sheets obtained through rapid heating of the ultrathin $In(OH)_3$ sheets in air: (C) TEM image; (D) HRTEM image; (E) AFM image; and (F) the corresponding height profiles; the numbers from 1 to 3 in (F) correspond to the numbers from 1 to 3 in (E).

formation of In_2O_3 with a porous structure and O-vacancies (Figures 2A and S3B).

By taking the products obtained by fast-heating the ultrathin $In(OH)_3$ sheets in air as an example, their XRD pattern in Figure S4 could be readily indexed to the cubic In_2O_3 (JCPDS NO. 88-2160). Also, the fast-heating strategy removes the oleate ions on the surface of the final In_2O_3 products, which could be confirmed by the corresponding IR spectra in Figure S3A, suggesting the formation of clean In_2O_3. The TEM image in Figure 2C clearly shows their sheet-like morphology, while the HRTEM in Figure 2D demonstrates their high orientation along the [01−1] projection. The atomic force microscopic (AFM) image and the corresponding height profiles in Figure 2E−F show their average thickness of ca. 0.9 nm, which agrees well with the 0.88 nm thickness of a 5-atom-thick In_2O_3 slab along the [01−1] direction. The TEM and AFM images in Figure 2C and E reveal the presence of abundant pores in the ultrathin In_2O_3 sheets, verified by the height profiles in Figure 2F.

To shed light on the correlation between O-vacancies and photocatalysis, the ultrathin In_2O_3 porous sheets with different O-vacancy concentrations are obtained by rapidly heating the ultrathin $In(OH)_3$ sheets in air and oxygen atmospheres, owing to the fact that the phase transformation from $In(OH)_3$ to In_2O_3 can introduce the O-vacancies.[4a] The 3d core level spectra in Figure 3B show two peaks located at 444.5 and 452.0 eV, which could be attributed to the characteristic spin−orbit split $3d_{5/2}$ and $3d_{3/2}$.[4a] Two peaks can also be clearly identified from the O 1s core level spectra shown in Figure 3A: one peak at 529.8 eV is

dx.doi.org/10.1021/ja501866r | J. Am. Chem. Soc. 2014, 136, 6826−6829

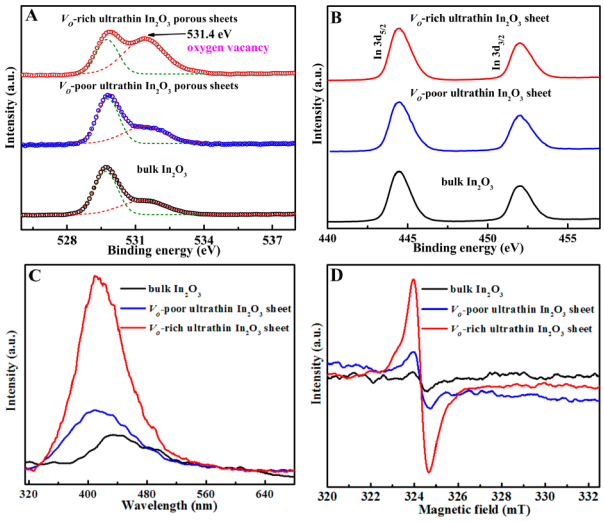

Figure 3. Characterizations for V_O-rich ultrathin In_2O_3 porous sheets, V_O-poor ultrathin In_2O_3 porous sheets, and bulk counterpart: (A) the O 1s XPS spectra and (B) In 3d core level spectra; (C) room-temperature photoluminescence spectra; (D) electron spin resonance spectra.

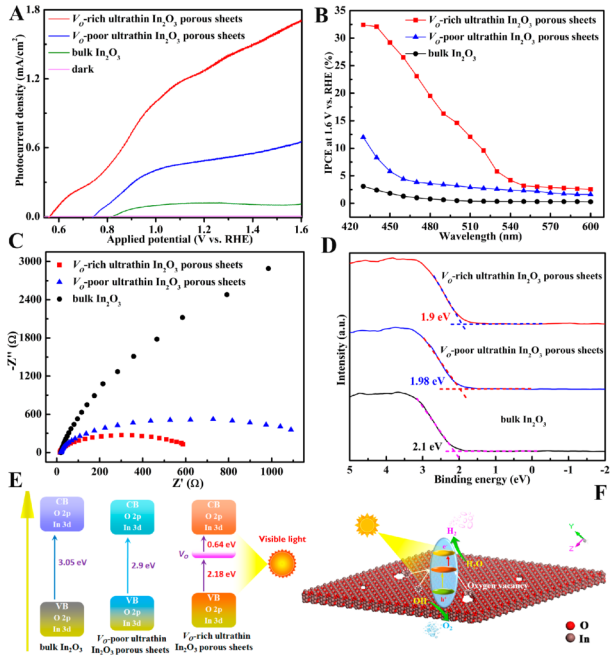

Figure 4. (A) Photocurrent vs applied potential curves under 300 W Xe lamp irradiation (λ > 420 nm); (B) IPCE at 1.6 V vs RHE; (C) electrochemical impedance spectra at 1.6 V vs RHE under 300 W Xe lamp irradiation (λ > 420 nm); (D) valence band XPS spectra; (E) schematic band structure obtained according to the results in (D) and Figure S6B; (F) schematic solar water splitting of V_O-rich ultrathin In_2O_3 porous sheets.

deemed as the oxygen bond of In−O−In, while the other located at 531.4 eV can be attributed to the O-atoms in the vicinity of an O-vacancy.[4a,13a] However, their peak area of 531.4 eV is widely different, which indicates that the atomically thin In_2O_3 porous sheets obtained in air possess much more O-vacancies compared with the atomically thin In_2O_3 porous sheets obtained in the O-atmosphere and bulk counterpart (Figure S5), while the last two products exhibit similar concentrations of O-vacancies. Moreover, the PL emission peak at 435 nm for bulk In_2O_3 could be mainly ascribed to the recombination of the photogenerated hole with the two-electron-trapped O-vacancy, while the blue-shifted peak at 410 nm for the ultrathin In_2O_3 porous sheets could be mainly attributed to the recombination of the photogenerated hole with the single-electron-trapped O-vacancy.[13b] Also, Figure 3C reveals that the atomically thin In_2O_3 porous sheets obtained in air possesses higher PL intensity compared with the atomically thin In_2O_3 porous sheets obtained in the O-atmosphere and bulk counterpart, suggesting their higher O-vacancy concentration, which is fairly consistent with the XPS analysis results in Figure 3A. Furthermore, all three In_2O_3 samples exhibit an ESR signal at g = 2.004 (Figure 3D), which could be identified as the electrons trapped on O-vacancies.[14] The signal intensity illustrates that the atomically thin In_2O_3 porous sheets obtained in air possess the highest O-vacancy concentration among the three In_2O_3 samples, while the other two samples exhibit similar O-vacancy concentrations, which agrees well with the XPS and PL results in Figure 3A and C.

To disclose the role of O-vacancies confined in ultrathin sheets in affecting photocatalysis, it is indispensable to implement the solar water splitting properties of V_O-rich ultrathin In_2O_3 porous sheets, V_O-poor ultrathin In_2O_3 porous sheets, and bulk counterpart. In fact, the above three In_2O_3-based photoelectrodes show the negligible dark currents of <5 μA/cm^2 at the overall applied potentials. Upon visible-light irradiation of a 300 W Xe lamp, the V_O-poor ultrathin In_2O_3 porous sheets-based photoelectrode possesses obviously increased photocurrent densities compared to the bulk In_2O_3-based photoelectrode (Figure 4A), suggesting the higher photoactivity of the ultrathin 2D In_2O_3 porous sheets. More intriguingly, the V_O-rich ultrathin In_2O_3 porous sheets-based photoelectrode shows further improved photocurrents compared to the V_O-poor ultrathin In_2O_3 porous sheets-based photoelectrode over all the applied potentials. For instance, at 1.6 V vs RHE, the V_O-rich ultrathin In_2O_3 porous sheets-based photoelectrode achieves a photocurrent density of 1.73 mA/cm^2, over 2.5 times larger than that of the V_O-poor ultrathin In_2O_3 porous sheets-based photoelectrode (Figure 4A), demonstrating the superiority of O-vacancies confined in the ultrathin 2D structure for promoting solar water splitting. In addition, the negative onset potential for the V_O-rich ultrathin In_2O_3 porous sheets indicates larger accumulation of electrons along with decreased charge recombination in their photoelectrode, fairly consistent with the increased DOS near the VBM resulting from the presence of O-vacancies. Moreover, Figure 4B reveals that the IPCE of the V_O-rich ultrathin In_2O_3 porous sheets-based photoelectrode is 32.3% at 450 nm, higher than 12% and 3% for the V_O-poor ultrathin In_2O_3 porous sheets- and bulk In_2O_3-based photoelectrodes. Furthermore, the V_O-rich/-poor ultrathin In_2O_3 porous sheets-based photoelectrodes exhibit negligible photocurrent variations after 7200 s of irradiation (Figure S6A), while the bulk In_2O_3-based photoelectrode shows obvious I−t fluctuations, implying the former's improved photostability.

Notably, the superior visible light water splitting efficiency of the V_O-rich ultrathin In_2O_3 porous sheets could be attributed to the synergistic effect between the ultrathin 2D structure and the O-vacancies confined in the ultrathin sheets. The ultrathin thickness and huge specific surface area enable the ultrathin In_2O_3 porous sheets to possess tight contact with the substrate and hence possesses lower interfacial resistance,[15] confirmed by the corresponding electrochemical impedance spectra in Figure 4C. In addition, the calculated results in Figure 1A−B reveal that the presence of O-vacancies endows the ultrathin In_2O_3 2D

dx.doi.org/10.1021/ja501866r | J. Am. Chem. Soc. 2014, 136, 6826−6829

structure with increased DOS at VBM, which ensures a higher carrier concentration and hence increase the electric field in the space charge regions, thus achieving enhanced carrier separation.[16] Importantly, UV−vis diffuse reflectance spectra and valence band XPS spectra in Figures S6B and 4D illustrate that the V_O-rich ultrathin In_2O_3 porous sheets exhibit a narrowed band gap from 2.90 to 2.18 eV compared with the V_O-poor ultrathin In_2O_3 porous sheets. This indicates that the O-vacancies contribute to shifting the onset light absorption from the UV to visible region, which could be ascribed to the appearance of a new defect level in the oxygen-defect 5-atom-thick In_2O_3 slab (Figures 1A and 4E). As such, the increased visible light absorption of the V_O-rich ultrathin In_2O_3 porous sheets could be attributed to the electron transition from the valence band to the new defect level or from the defect level to the conduction band (Figure 4E−F).[4a]

In summary, O-vacancies confined in atomically thin sheets are first presented as an ideal material model for disclosing the role of O-vacancies in photocatalysis. As an example, 5-atom-thick In_2O_3 porous sheets with rich/poor O-vacancies are first successfully synthesized by rapidly heating the intermediate of ultrathin $In(OH)_3$ sheets, which are fabricated by virtue of an artificial hexagonal mesostructured In-oleate complex. All the XPS, PL, and ESR spectra demonstrate the different O-vacancy concentrations in the defect-rich/-poor ultrathin In_2O_3 porous sheets and bulk counterpart and, hence, provide three ideal material models for studying the O-vacancy−photocatalysis relationship. Moreover, first principle calculations disclose that the O-vacancies lead the 5-atom-thick In_2O_3 sheets to possess a new donor level near CBM and a higher DOS at VBM, which endow them with a narrowed band gap and higher carrier concentration, hence facilitating the visible light harvesting and the carrier separation efficiency. As a result, the V_O-rich ultrathin In_2O_3 porous sheets-based photoelectrode exhibits a visible light photocurrent of 1.73 mA/cm^2, over 2.5 and 15 times larger than that of the V_O-poor ultrathin In_2O_3 porous sheets- and bulk In_2O_3-based photoelectrodes. Briefly, this work not only develops a mesoscopic-assembly strategy for fabricating non-layered atomically thin sheets but also theoretically/experimentally demonstrates atomic-level insights into the role of O-vacancies in promoting water splitting efficiency.

■ ASSOCIATED CONTENT

Supporting Information

Experimental procedures, computational details, and additional figures. This material is available free of charge via the Internet at http://pubs.acs.org.

■ AUTHOR INFORMATION

Corresponding Authors

yxie@ustc.edu.cn
yfsun@ustc.edu.cn

Notes

The authors declare no competing financial interest.

■ ACKNOWLEDGMENTS

This work was financially supported by National Nature Science Foundation (21331005, 11079004, 90922016, 21201157, 11321503), Chinese Academy of Science (XDB01020300), Program for New Century Excellent Talents in University (NCET-13-0546), and the Fundamental Research Funds for the Central Universities (WK2060190027).

■ REFERENCES

(1) (a) Fujishima, A.; Honda, K. *Nature* **1972**, *238*, 37. (b) Kudo, A.; Miseki, Y. *Chem. Soc. Rev.* **2009**, *38*, 253. (c) Sun, Y. F.; Sun, Z. H.; Gao, S.; Cheng, H.; Liu, Q. H.; Piao, J. Y.; Yao, T.; Wu, C. Z.; Hu, S. L.; Wei, S. Q.; Xie, Y. *Nat. Commun.* **2012**, *3*, 1057. (d) Sun, Y. F.; Cheng, H.; Gao, S.; Sun, Z. H.; Liu, Q. H.; Liu, Q.; Lei, F. C.; Yao, T.; He, J. F.; Wei, S. Q.; Xie, Y. *Angew. Chem., Int. Ed.* **2012**, *51*, 8727. (e) Sun, Y. F.; Sun, Z. H.; Gao, S.; Cheng, H.; Liu, Q. H.; Lei, F. C.; Wei, S. Q.; Xie, Y. *Adv. Energy Mater.* **2014**, *4*, 1300611.

(2) (a) Zhang, J.; Yu, J. G.; Zhang, Y. M.; Li, Q.; Gong, J. R. *Nano Lett.* **2011**, *11*, 4774. (b) Hoang, S.; Guo, S. W.; Hahn, N. T.; Bard, A. J.; Mullins, C. B. *Nano Lett.* **2012**, *12*, 26. (c) Sun, Y. F.; Qu, B. Y.; Liu, Q.; Gao, S.; Yan, Z. X.; Yan, W. S.; Pan, B. C.; Wei, S. Q.; Xie, Y. *Nanoscale* **2012**, *4*, 3761.

(3) (a) Chen, X. B.; Liu, L.; Yu, P. Y.; Mao, S. S. *Science* **2011**, *331*, 746. (b) Naldoni, A.; Allieta, M.; Santangelo, S.; Marelli, M.; Fabbri, F.; Cappelli, S.; Bianchi, C. L.; Psaro, R.; Santo, V. D. *J. Am. Chem. Soc.* **2012**, *134*, 7600. (c) Wang, J. P.; Wang, Z. Y.; Huang, B. B.; Ma, Y. D.; Liu, Y. Y.; Qin, X. Y.; Zhang, X. Y.; Dai, Y. *ACS Appl. Mater. Interfaces* **2012**, *4*, 4024. (d) Lu, X. H.; Zeng, Y. X.; Yu, M. H.; Zhai, T.; Liang, C. L.; Xie, S. L.; Balogun, M. S.; Tong, Y. X. *Adv. Mater.* **2014**, DOI: 10.1002/adma.201305851. (e) Li, M. Y.; Hu, Y.; Xie, S. L.; Huang, Y. C.; Tong, Y. X.; Lu, X. H. *Chem. Commun.* **2014**, *50*, 4341.

(4) (a) Gan, J. Y.; Lu, X. H.; Wu, J. H.; Xie, S. L.; Zhai, T.; Yu, M. H.; Zhang, Z. S.; Mao, Y. C.; Wang, S. C. L.; Shen, Y.; Tong, Y. X. *Sci. Rep.* **2013**, *3*, 1021. (b) Sun, M.; Xiong, S. J.; Wu, X. L.; He, C. Y.; Li, T. H.; Chu, P. K. *Adv. Mater.* **2013**, *25*, 2035. (c) Yang, H. X.; Liu, L.; Liang, H.; Wei, J. J.; Yang, Y. Z. *CrystEngComm* **2011**, *13*, 5011. (d) Ho, C. H.; Chan, C. H.; Tien, L. C.; Huang, Y. S. *J. Phys. Chem. C* **2011**, *115*, 25088. (e) Gan, J. Y.; Lu, X. H.; Zhai, T.; Zhao, Y. F.; Xie, S. L.; Mao, Y. C.; Zhang, Y. L.; Yang, Y. Y.; Tong, Y. X. *J. Mater. Chem.* **2011**, *21*, 14685. (f) Meng, M.; Wu, X. L.; Zhu, X. B.; Zhu, X. S.; Chu, P. K. *ACS Appl. Mater. Interfaces* **2014**, *6*, 4081.

(5) Sun, Y. F.; Gao, S.; Xie, Y. *Chem. Soc. Rev.* **2014**, *43*, 530.

(6) Lany, S.; Zakutayev, A.; Mason, T. O.; Wager, J. F.; Poeppelmeier, K. R.; Perkins, J. D.; Berry, J. J.; Ginley, D. S.; Zunger, A. *Phys. Rev. Lett.* **2012**, *108*, 016802.

(7) Sun, Y. F.; Liu, Q. H.; Gao, S.; Cheng, H.; Lei, F. C.; Sun, Z. H.; Jiang, Y.; Su, H. B.; Wei, S. Q.; Xie, Y. *Nat. Commun.* **2013**, *4*, 2899.

(8) Sun, Y. F.; Lei, F. C.; Gao, S.; Pan, B. C.; Zhou, J. F.; Xie, Y. *Angew. Chem., Int. Ed.* **2013**, *52*, 10569.

(9) (a) Schliehe, C.; Juarez, B. H.; Pelletier, M.; Jander, S.; Greshnykh, D.; Nagel, M.; Meyer, A.; Foerster, S.; Kornowski, A.; Klinke, C.; Weller, H. *Science* **2010**, *329*, 550. (b) Li, B. X.; Xie, Y.; Jing, M.; Rong, G. X.; Tang, Y. C.; Zhang, G. Z. *Langmuir* **2006**, *22*, 9380.

(10) Huo, Z. Y.; Tsung, C. K.; Huang, W. Y.; Fardy, M.; Yan, R. X.; Zhang, X. F.; Li, Y. D.; Yang, P. D. *Nano Lett.* **2009**, *9*, 1260.

(11) Penn, L.; Banfield, J. F. *Science* **1998**, *281*, 969.

(12) Sun, Y. F.; Xie, Y.; Wu, C. Z.; Zhang, S. D.; Jiang, S. S. *Nano Res.* **2010**, *3*, 620.

(13) (a) Banger, K. K.; Yamashita, Y.; Mori, K.; Peterson, R. L.; Leedham, T.; Rickard, J.; Sirringhaus, H. *Nat. Mater.* **2012**, *10*, 45. (b) Huang, G. S.; Wu, X. L.; Mei, Y. F.; Shao, X. F. *J. Appl. Phys.* **2003**, *93*, 582.

(14) Nakamura, I.; Negishi, N.; Kutsuna, S.; Ihara, T.; Sugihara, S.; Takeuchi, E. *J. Mol. Catal. A: Chem.* **2000**, *161*, 205.

(15) (a) Sun, Y. F.; Cheng, H.; Gao, S.; Liu, Q. H.; Sun, Z. H.; Xiao, C.; Wu, C. Z.; Wei, S. Q.; Xie, Y. *J. Am. Chem. Soc.* **2012**, *134*, 20294. (b) Sun, Y. F.; Zhu, J. B.; Bai, L. F.; Li, Q. Y.; Zhang, X.; Tong, W.; Xie, Y. *Inorg. Chem. Front.* **2014**, *1*, 58.

(16) (a) Klahr, B. M.; Hamann, T. W. *Appl. Phys. Lett.* **2011**, *99*, 063508. (b) Hamann, T. W. *Dalton Trans.* **2012**, *41*, 7830.